

Generation of 280 THz-spanning near-ultraviolet light in lithium niobate-on-insulator waveguides with sub-100 pJ pulses

Journal Article

Author(s):

[Reig Escalé, Marc](#) ; Kaufmann, Fabian; Jiang, Hehai; Pohl, David; [Grange, Rachel](#) 

Publication date:

2020-12

Permanent link:

<https://doi.org/10.3929/ethz-b-000458295>

Rights / license:

[Creative Commons Attribution 4.0 International](#)

Originally published in:

APL Photonics 5(12), <https://doi.org/10.1063/5.0028776>

Funding acknowledgement:

179099 - Nonlinear Perovskite Nanomaterials for Metasurfaces and Integrated Photonics (SNF)
714837 - Second-Order Nano-Oxides for Enhanced Nonlinear Photonics (EC)

Generation of 280 THz-spanning near-ultraviolet light in lithium niobate-on-insulator waveguides with sub-100 pJ pulses EP

Cite as: APL Photonics 5, 121301 (2020); <https://doi.org/10.1063/5.0028776>

Submitted: 07 September 2020 . Accepted: 19 November 2020 . Published Online: 07 December 2020

 Marc Reig Escalé,  Fabian Kaufmann, Hehai Jiang,  David Pohl, and  Rachel Grange

COLLECTIONS

EP This paper was selected as an Editor's Pick



View Online



Export Citation




CrossMark

ARTICLES YOU MAY BE INTERESTED IN

[Low-loss low thermo-optic coefficient Ta₂O₅ on crystal quartz planar optical waveguides](#)
APL Photonics 5, 116103 (2020); <https://doi.org/10.1063/5.0024743>

[Alumina coating for dispersion management in ultra-high Q microresonators](#)
APL Photonics 5, 116107 (2020); <https://doi.org/10.1063/5.0028839>

[Terahertz optical machine learning for object recognition](#)
APL Photonics 5, 126103 (2020); <https://doi.org/10.1063/5.0029310>



AMERICAN ELEMENTS
THE ADVANCED MATERIALS MANUFACTURER®

additive manufacturing epitaxial crystal growth cerium oxide polishing powder silver nanoparticles sputtering targets III-IV semiconductors CVD precursors europium phosphors

deposition slugs OLED Lighting spintronics solar energy osmium nanoribbons thin films chalcogenides AuNPs

GDC Li-ion battery electrolytes 99.999% ruthenium spheres

endohedral fullerenes copper nanoparticles diamond micropowder

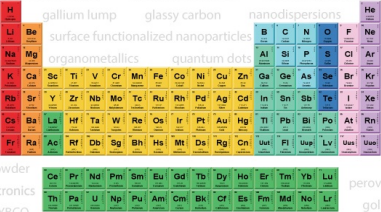
CIGS MBE grade materials palladium catalysts flexible electronics

beta-barium borate borosilicate glass dysprosium pellets YBCO

pyrolytic graphite 3d graphene foam indium tin oxide mesoporous silica

raman substrates sapphire windows tungsten carbide InGaAs

barium fluoride carbon nanotubes lithium niobate scandium powder



gallium lump glassy carbon nanodispersions

surface functionalized nanoparticles organometallics quantum dot

III-IV semiconductors laser crystals ultra high purity materials MOFs

rare earth metals photovoltaics refractory metals MOCVD

superconductors transparent ceramics ultra high purity silicon

*American Elements opens up a world of possibilities so you can **Now Invent!***

Over 15,000 certified high purity laboratory chemicals, metals, & advanced materials and a state-of-the-art Research Center. Printable GHS-compliant Safety Data Sheets. Thousands of new products. And much more. All on a secure multi-language 'Mobile Responsive' platform.

perovskite crystals yttrium iron garnet alternative energy h-BN

gold nanocubes graphene oxide macromolecules photonics

rhodium sponge fiber optics beamsplitters infrared dyes zeolites

fused quartz metallocenes platinum ink buckyballs Ti-6Al-4V

Now Invent.™
The Next Generation of Material Science Catalogs

www.americanelements.com



Generation of 280 THz-spanning near-ultraviolet light in lithium niobate-on-insulator waveguides with sub-100 pJ pulses

Cite as: APL Photon. 5, 121301 (2020); doi: 10.1063/5.0028776
Submitted: 7 September 2020 • Accepted: 19 November 2020 •
Published Online: 7 December 2020



Marc Reig Escalé,^{1,a)}  Fabian Kaufmann,¹  Hehai Jiang,^{1,2}  David Pohl,¹  and Rachel Grange¹ 

AFFILIATIONS

¹Optical Nanomaterial Group, Institute for Quantum Electronics, Department of Physics, ETH Zurich, Auguste-Piccard-Hof 1, 8093 Zurich, Switzerland

²Bindley Bioscience Center, Purdue University, 1203 W. State St., West Lafayette, Indiana 47907, USA

^{a)}Author to whom correspondence should be addressed: marcre@phys.ethz.ch

ABSTRACT

Integrated optics has weak ultraviolet and near-ultraviolet (NUV) light conversion due to its strong material dispersion and large propagation losses. To reach this spectral range, we use non-centrosymmetric waveguides that convert near-infrared (NIR) supercontinuum light into broadband NUV light. We measure a 280 THz span that reaches the upper frequency of 851 THz (352 nm) in a 14-mm long rib waveguide of lithium niobate-on-insulator, with an engineered dispersion for supercontinuum generation in the NIR range. The results on broadband NUV signals promote integrated optics for spectroscopy and fluorescence applications such as atomic clocks and chemical sensors.

© 2020 Author(s). All article content, except where otherwise noted, is licensed under a Creative Commons Attribution (CC BY) license (<http://creativecommons.org/licenses/by/4.0/>). <https://doi.org/10.1063/5.0028776>

I. INTRODUCTION

The field of supercontinuum generation (SCG) evolved from first observations in bulk silica¹ to applications in standard silica and photonic fibers.^{2,3} In later years, integrated photonics has demonstrated octave-spanning SCG in CMOS-compatible, dispersion-engineered sub-micron silicon nitride (SiN) waveguides operating in the visible (VIS), short-wave infrared (SWIR) and mid-infrared (MIR) regimes^{4–6} as well as in silicon (Si) waveguides in the SWIR and MIR regimes.^{7,8}

While SiN and Si can generate octave-spanning SCG, the resulting spectra are typically centered around the pump wavelength. Using non-centrosymmetric materials with a non-vanishing $\chi^{(2)}$ -tensor allows extending the continuum into the blue by use of cascaded second-harmonic generation while pumping at near-infrared (NIR) or SWIR wavelengths. Recent results expand this to the near-ultraviolet (NUV) range in waveguides of aluminum nitride either by pumping at 1560 nm⁹ or at 780 nm¹⁰ with a non-linearity of $|d_{33}| \sim 8.4$ pm/V,¹¹ showing a frequency comb spanning of more than 100 THz. Such devices are interesting for a range of frequency comb applications such as atomic clocks^{12–14} or quantum memories.^{15,16}

Another non-centrosymmetric material is lithium niobate, which possesses a non-linearity of $|d_{33}| \sim 33$ pm/V¹⁷ and exhibits a transparency window in the range of ~ 330 nm–4500 nm.^{18–20} Bulk optical lithium niobate waveguides are mostly fabricated by titanium in-diffusion^{21–23} or proton exchange methods.^{24–27} In such waveguide systems, octave-spanning SCG has been shown in periodically poled devices operating in the SWIR and MIR regimes.^{28–30} However, these systems have a low index contrast that diminishes the optical confinement and use pulse energies larger than 1 nJ.

For smaller pulse energies, stronger optical confinement is required. The lithium niobate-on-insulator (LNOI) platform typically consists of a <600 nm lithium niobate thin-film bonded onto an oxide layer that results in a refractive index contrast of $\Delta n \sim 0.7$. LNOI combines the non-linearities of lithium niobate with high modal confinement in sub-micron waveguides,^{31–33} which enables dispersion engineering.^{34–36} Octave-spanning SCG has already been shown on the LNOI platform,^{37–39} but so far, broadening the optical spectrum in the NUV region has not been the focus.

Here, we optimize the group velocity dispersion (GVD) in the NIR range for an LNOI waveguide with a cross section of 700×400 nm². After dispersion optimization, we pump a 14 mm-long

waveguide at 950 nm with 220 fs pulses and a low pulse energy of 67 pJ in the waveguide (peak power of 266 W). We report a broadening of the NIR pump signal of $\Delta\lambda_{NIR} = 518$ nm ($\Delta\omega_{NIR} = 179$ THz), and by second-harmonic generation, this NIR SCG signal results in cascaded SCG with a NUV bandwidth of $\Delta\lambda_{NUV} = 173$ nm ($\Delta\omega_{NUV} = 280$ THz). In addition, by selecting the pump wavelength within the range of 940 nm–1000 nm, we tailor the cascaded SCG from the NUV toward the VIS range.

II. SAMPLE AND SETUP DESCRIPTION

Figures 1(a) and 1(b) show an x-cut LNOI rib waveguide with a top width of 700 nm, ridge-height of 250 nm, and remaining thin-film thickness of 150 nm. The waveguide is fabricated using standard e-beam lithography and optimized ICP/RIE dry-etching. Subsequent wet-etching in a buffered oxide etch (BOE) and potassium hydroxide (KOH) removes the remaining mask and dry-etching residuals. Figure 1(c) shows the input side of a set of 14 mm-long waveguides.

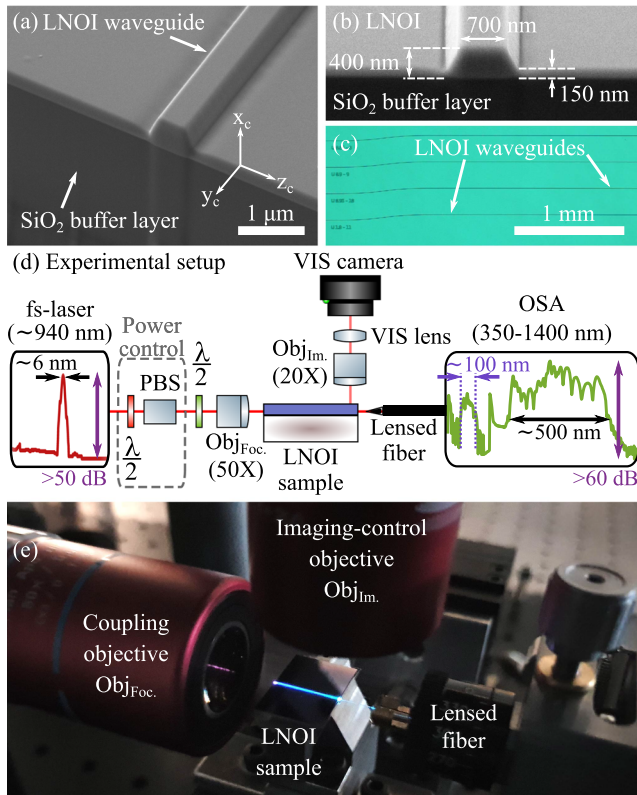


FIG. 1. [(a) and (b)] Scanning electron microscopy (SEM) image of the device showing the 700 nm × 400 nm trapezoidal waveguide with a sidewall angle of 60° and remaining thin-film thickness of 150 nm, which results in a ridge-height of 250 nm, (c) the optical microscope image of the LNOI chip, (d) the experimental setup, where a femtosecond-laser and free-space objective are used for light coupling and a lensed fiber and an optical spectrum analyzer are used for broadband detection (350 nm–1700 nm), and (e) the picture showing a single LNOI waveguide pumped at 950 nm. The blue and white light result from the SCG process.

Figure 1(d) depicts the experimental setup, which consists of a femtosecond (fs) pulsed oscillator with an 80 MHz pulse-train at 950 nm and a pulse width of 220 fs together with a power control unit consisting of a polarization beam splitter plus a half-wave plate. We use a half-wave plate to control the polarization of the fs pulses, which are then focused onto the LNOI sample by a 50× focusing objective with 11.2 dB/facet coupling losses. After collection of the optical signal with a lensed fiber (Oz Optics TPMJ-3A-1550-8), the optical signal is sent to an optical spectrum analyzer (OSA, Advantest Q8381A) with a detection range from 350 nm to 1750 nm and the same resolution of 5 nm over the full wavelength span. One measurement covers the spectral broadening in the NIR and the cascaded spectral broadening in the NUV, close to the bandgap of lithium niobate.^{18–20} The 20× imaging objective is used for sample positioning and alignment in combination with a VIS lens and camera. Figure 1(e) shows the chip mounted on a vacuum chuck within the experimental setup, with blue and white light resulting from the SCG process.

III. WAVEGUIDE DISPERSION ENGINEERING

In waveguides with high modal confinement, the material dispersion $\propto dn/d\lambda$ can be compensated with the waveguide dispersion $\propto dn_{eff}/d\lambda$ that arises from engineering the waveguide cross section. Here, $n(n_{eff})$ is the (effective) refractive index of the guiding medium, and λ is the wavelength of the light. Using the waveguide dispersion, one can achieve a net anomalous dispersion in the system. In photonic integrated circuits, this method was originally implemented in Si and SiN waveguides^{40,41} and is also applicable for the LNOI platform.^{34–36}

The waveguide dispersion is more commonly given in frequency space as the group velocity dispersion (GVD),

$$GVD(\omega_P) \equiv \beta_2 = \frac{\partial^2 \beta}{\partial \omega^2} \Big|_{\omega=\omega_P},$$

with $\beta = k_0 \cdot n_{eff}$ and ω_P being the pump frequency, related by $\omega_P = \frac{2\pi c}{\lambda_P}$ to the pump wavelength λ_P . As shown in Fig. 2(a), we use finite element method (FEM) simulations to calculate and maximize the anomalous dispersion range ($GVD < 0$) of the fundamental mode at 950 nm in a 700 × 400 nm² trapezoidal waveguide with sidewall angles of 60° and a remaining thin-film thickness of 150 nm.

Figure 2(a) shows the calculated anomalous and normal GVD of the TM₀₀ and TE₀₀ modes. Here, we select the TM₀₀ optical mode with two zero-crossings at 730 nm and 1040 nm that ensure the presence of dispersive waves at both ends of the spectrum, provided the pump wavelength is in the anomalous dispersion regime. The goal is to have a broad spectrum in the NIR that in turn generates a broad signal in the NUV through cascaded second-harmonic generation, which we refer to as cascaded SCG.

To select the broadest dispersion regime, we now maximize the bandwidth of the dispersion operator,^{42,43}

$$\hat{D}(\omega) = \sum_{n \geq 2} \frac{\beta_n(\omega_P)}{n!} (\omega - \omega_P)^n,$$

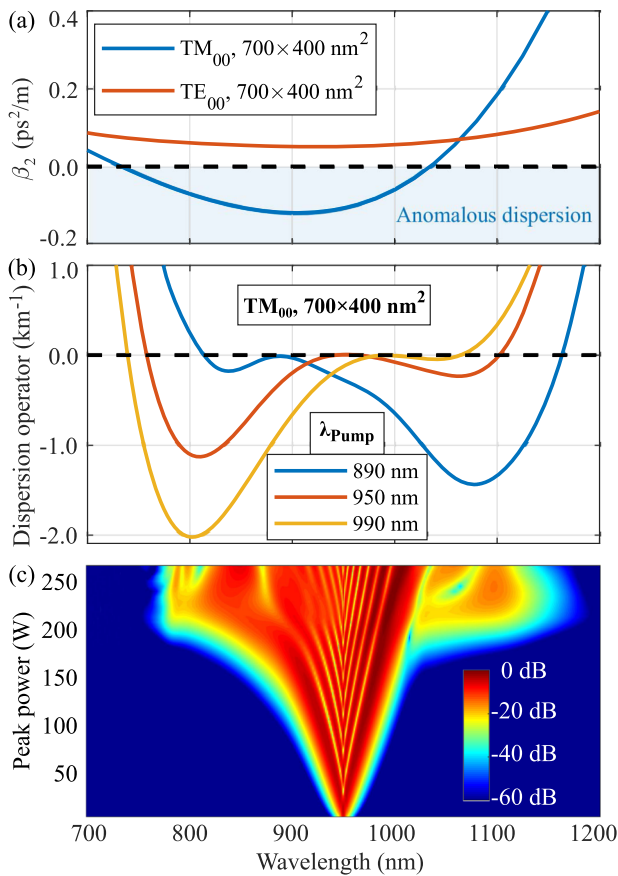


FIG. 2. (a) GVD for the quasi TM₀₀ and TE₀₀ modes in a waveguide with a top-width of 700 nm, ridge height of 250 nm, and sidewall angle of 60°. Only the TM₀₀ mode experiences anomalous dispersion (GVD < 0, blue-shaded region), (b) the dispersion operator \hat{D} for different pump wavelengths λ_p and the same waveguide geometry, and (c) simulated output spectra at different peak powers.

where $\beta_n = \frac{\partial^n \beta}{\partial \omega^n}$, with respect to the pump frequency ω_p . The zero-crossings of \hat{D} allow us to visualize the dispersive waves and therefore the NIR broadening of the SCG. Figure 2(b) shows the calculated dispersion operator \hat{D} of the TM₀₀ mode for different pump wavelengths. We select the pump wavelength of 950 nm since it maximizes the spectral separation of the dispersive waves, which are located at 760 nm and 1100 nm. To support the dispersive wave calculations, we use the split-step Fourier method to simulate the generalized nonlinear Schrödinger equation.^{5,42,43} Figure 2(c) shows the computed output optical spectra depending on the input peak power, where the dispersive waves appear at a peak power of ~200 W at wavelengths of 790 nm and 1120 nm, a deviation of 3.9% and 1.8% from the results shown in Fig. 2(b).

IV. NIR AND NUV SPECTRAL BROADENINGS

Figure 3 shows the generation of the SCG pumped at $\lambda_p = 950$ nm and the cascaded SCG at $\lambda_p/2 = 475$ nm for pulse energies

ranging from 13 pJ to 67 pJ in the waveguide, which corresponds to peak powers inside the waveguide from 53 W to 266 W. The broadening of the NIR pump increases for increasing pulse energy largely due to self-phase modulation until the appearance of dispersive waves with a pulse energy of 53 pJ and a 30 dB-NIR bandwidth of $\Delta\lambda_{NIR} = 278$ nm ($\Delta\omega_{NIR} = 94$ THz), while for a pulse energy of 67 pJ, we measure a 30 dB-NIR bandwidth of $\Delta\lambda_{NIR} = 518$ nm ($\Delta\omega_{NIR} = 179$ THz). We observe the dispersive waves at 725 nm and 1175 nm, which deviate by 4.6% and 6.4% from the results shown in Fig. 2(b), respectively. We attribute this difference to the trenching of the LNOI waveguides and the ± 20 nm thickness variation of the thin-film over the full chip. The trenches can be observed in Fig. 1(b) between the waveguide sidewall and the remaining thin-film. Trenching is a by-product of the dry-etching that we employ to fabricate the LNOI waveguides. The dry-etching causes redeposition, which leads to the appearance of trenches. The redeposition rate differs from the edge of the sample to the center of it, which translates into inhomogeneous trenches. The inhomogeneous trenching slightly modifies the cross section, which in turn affects the dispersion operator and the spectral location of the dispersive waves.

The onset of the self-phase modulation at 27 pJ for both pump and SHG signals shows the cascaded nature of the process, and the broadening of the SHG signal is consistent with the SCG broadening in the NIR range. For 67 pJ, the NUV signal extends to the short-wavelength side down to 352 nm, which is close to the bandgap of lithium niobate, and shows a 30 dB-NUV bandwidth of $\Delta\lambda_{NUV} = 173$ nm ($\Delta\omega_{NUV} = 280$ THz), which is more than two times broader than previous results.¹⁰ The dispersive waves limit the maximal spectral bandwidth; therefore, pulse energies higher than 53 pJ do not broaden the pump spectrum any further. The two kinks at wavelengths 580 nm and 1040 nm (clearly visible in the 27 pJ measurement of Fig. 3) are artifacts of the OSA.

The detected average power is ~ 3 μ W (-25 dBm) around the NIR pump wavelength of 950 nm. For NUV signals, we detect power levels of ~ 10 nW (-50 dBm) at a wavelength of 475 nm and 3.2 nW (-55 dBm) at 360 nm. The drop in detected powers between NIR and NUV ranges is ~ 25 dB, which suggests a more efficient broadband generation than power ratios of ~ 50 dB in LNOI waveguides that are pumped further in the SWIR range (~ 1500 nm).³⁸ In terms of narrowband SHG conversion efficiency, before self-phase modulation occurs, we estimate a conversion efficiency of only $\sim 1\%$ $W^{-1} cm^{-2}$, which is lower than the conversion efficiency of 4600% $W^{-1} cm^{-2}$ in periodically poled LNOI waveguides.⁴⁴ We expected this result since we engineered the dispersion to broaden the SCG pump spectrum, not to enhance the SHG modal phase matching of particular modes. Further work could optimize SHG phase matching by employing chirp-tapered waveguides,¹⁰ periodic modulations on the waveguide width,⁴⁵ or periodically poled lithium niobate thin-films.⁴⁶

We report an optical damage threshold to the LNOI waveguide input of ~ 8 kW peak power in the coupling process after >10 min of exposure, which agrees with previous results suggesting a >7 kW damage threshold in LNOI waveguides.³⁸ However, an exhaustive study on this topic as performed for bulk lithium niobate^{47–49} is still required. In addition, undoped LNOI waveguides exhibit a photorefractive effect in a fast response of ~ 21 ms in the NIR range, which is more than three orders of magnitude faster than that in bulk lithium

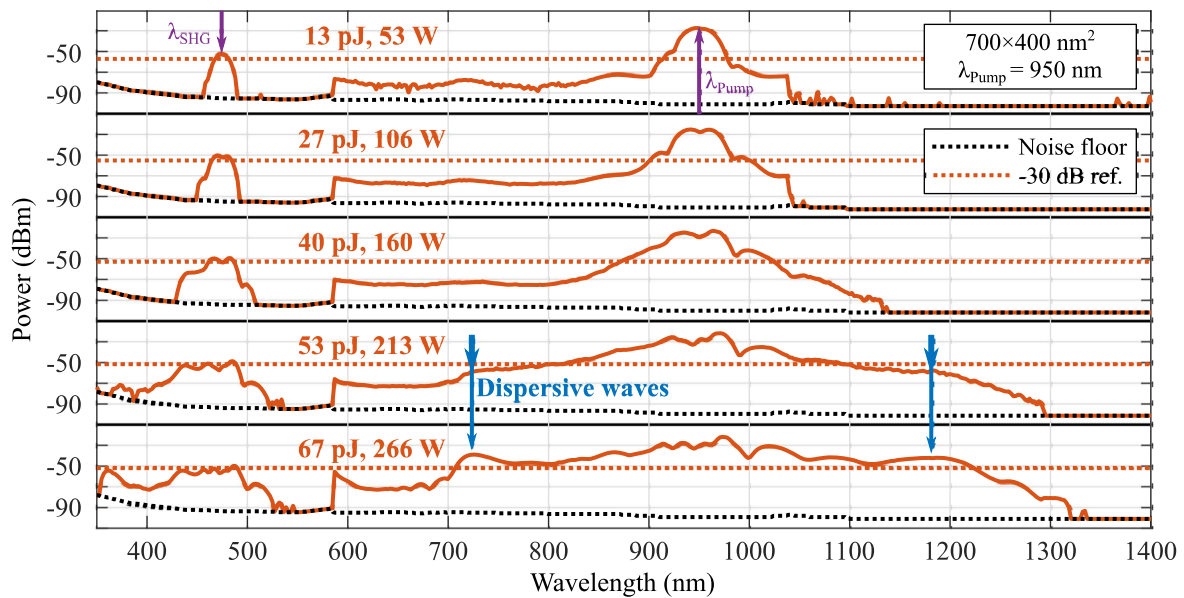


FIG. 3. Supercontinuum power spectra for different pulse energies in an LNOI waveguide with a top width of 700 nm and ridge height of 250 nm pumped at 950 nm. The dotted orange lines indicate the 30 dB-bandwidth for each generated signal, measured from each signal peak. The dotted black line denotes the noise floor of the optical spectrum analyzer. The blue arrows indicate the spectral location of the dispersive waves.

niobate devices.⁵⁰ Doping the lithium niobate thin-film with, for instance, magnesium would diminish the optical damage threshold in the VIS and NIR range, but the same might not apply to the NUV range.^{51,52}

All the optical spectra shown in Fig. 3 have a discontinuity between 550 nm and 580 nm. To overlap the NIR SCG with its

second-harmonic signal in the NUV range, the dispersion operator should become broader than that shown in Fig. 2(b), which can be achieved by increasing the index contrast between the waveguide and its surroundings. For that purpose, the LNOI waveguides can undergo a partial³⁷ or full³⁹ etching of the silicon dioxide buffer layer underneath the LNOI waveguide.

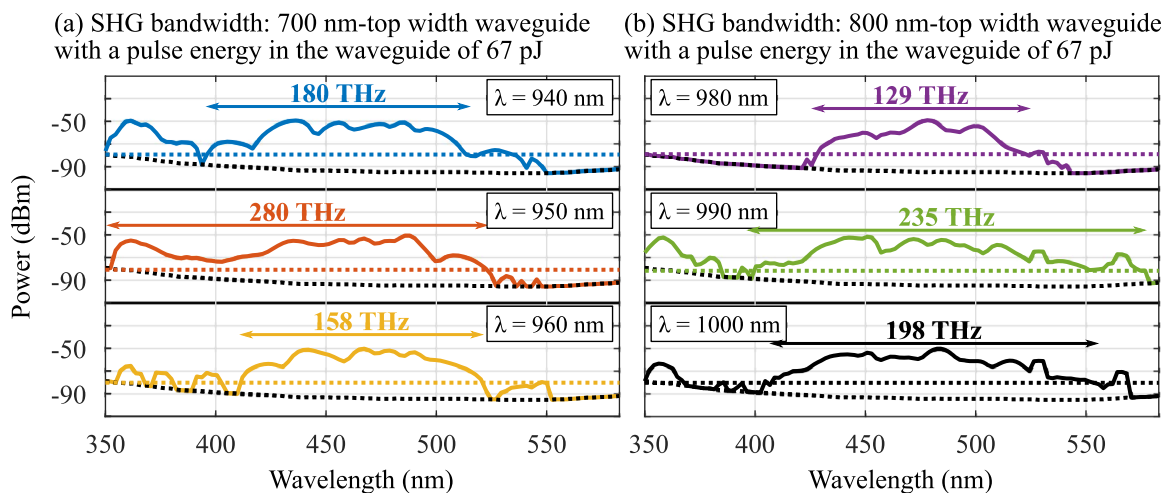


FIG. 4. (a) Cascaded supercontinuum generation (SCG) spectra through second-harmonic generation for an LNOI waveguide with a top width of 700 nm and ridge height of 250 nm for pump wavelengths of 940 nm, 950 nm, and 960 nm and (b) cascaded SCG of an LNOI waveguide with a top width of 800 nm and ridge height of 250 nm for pump wavelengths of 980 nm, 990 nm, and 1000 nm. The red detuning of the pump wavelengths of (b) compared to (a) is given by the red-shift in the dispersion operator of the 800 nm top-width waveguide. In both (a) and (b), the black-dotted line refers to the OSA noise floor while the colored-dotted line displays each respective 30 dB-bandwidth.

To better understand the behavior of NUV broadening, we conduct a wavelength sweep of the NIR pump from 940 nm to 960 nm. As shown in Fig. 2(b), the pump wavelength modifies the bandwidth of the dispersion operator, and hence, the SCG and its cascaded signal are also modified. Figure 4(a) shows the generated NUV supercontinuum spectra at different pump wavelengths for the same device as presented before. The corresponding 30 dB-bandwidths are highlighted, demonstrating the dependence on the pump wavelength, shown as expected in Fig. 2(b).

For a waveguide with a slightly larger cross section (800 nm top width and 250 nm ridge height), the dispersion operator is red-shifted with respect to the one shown in Fig. 2(b). Then, the optimal pump wavelength is also red-shifted, which Fig. 4(b) shows to be 990 nm (303 THz), with a broadening of $\Delta\lambda_{NUV} = 181$ nm ($\Delta\omega_{NUV} = 235$ THz) in the NUV regime. By selecting the waveguide cross section and pump wavelength, the broadening of the second-harmonic signal can be tailored to specific needs in the NUV or more toward the VIS range.

V. CONCLUSION

In a non-centrosymmetric LNOI waveguide, we demonstrated broad NUV generation through direct second-harmonic generation from SCG in the NIR range. The NUV signal has a 30 dB-bandwidth of 280 THz (173 nm) when pumped at 950 nm with a pulse energy of 67 pJ inside the waveguide. The results present sub-100 pJ, nonlinear systems as broadband NUV sources for NUV fluorescence and comb applications. However, since the generated NUV light is close to the bandgap of lithium niobate, doped lithium niobate thin-films (i.e., with magnesium) should be considered for mitigating the photorefractive effect in the VIS–NIR ranges even at pulse energies lower than 67 pJ.

AUTHORS' CONTRIBUTIONS

M.R.E. and F.K. equally contributed to this work.

ACKNOWLEDGMENTS

We acknowledge support for nanofabrication from the Scientific Center of Optical and Electron Microscopy (ScopeM) and from the cleanroom facilities BRNC and FIRST of ETH Zurich. This work was supported by the Swiss National Science Foundation, Grant No. 179099, and by the European Union's Horizon 2020 Research and Innovation Program from the European Research Council, under Grant Agreement No. 714837 (Chi2-nano-oxides).

DATA AVAILABILITY

The data that support the findings of this study are available from the corresponding author upon reasonable request.

REFERENCES

- R. R. Alfano and S. L. Shapiro, "Observation of self-phase modulation and small-scale filaments in crystals and glasses," *Phys. Rev. Lett.* **24**, 592–594 (1970).
- C. Lin and R. H. Stolen, "New nanosecond continuum for excited-state spectroscopy," *Appl. Phys. Lett.* **28**, 216–218 (1976).
- J. K. Ranka, R. S. Windeler, and A. J. Stentz, "Visible continuum generation in air-silica microstructure optical fibers with anomalous dispersion at 800 nm," *Opt. Lett.* **25**, 25–27 (2000).
- R. Halir, Y. Okawachi, J. S. Levy, M. A. Foster, M. Lipson, and A. L. Gaeta, "Ultra-broadband supercontinuum generation in a CMOS-compatible platform," *Opt. Lett.* **37**, 1685–1687 (2012).
- H. Zhao, B. Kuyken, S. Clemmen, F. Leo, A. Subramanian, A. Dhakal, P. Helin, S. Severi, E. Brainis, G. Roelkens, and R. Baets, "Visible-to-near-infrared octave spanning supercontinuum generation in a silicon nitride waveguide," *Opt. Lett.* **40**, 2177–2180 (2015).
- X. Liu, M. Pu, B. Zhou, C. J. Krückel, A. Fülöp, V. Torres-Company, and M. Bache, "Octave-spanning supercontinuum generation in a silicon-rich nitride waveguide," *Opt. Lett.* **41**, 2719–2722 (2016).
- N. Singh, M. Xin, D. Vermeulen, K. Shtyrkova, N. Li, P. T. Callahan, E. S. Magden, A. Ruocco, N. Fahrenkopf, C. Baiocco, B. P.-P. Kuo, S. Radic, E. Ippen, F. X. Kärtner, and M. R. Watts, "Octave-spanning coherent supercontinuum generation in silicon on insulator from 1.06 μm to beyond 2.4 μm ," *Light: Sci. Appl.* **7**, 17131 (2018).
- R. K. W. Lau, M. R. E. Lamont, A. G. Griffith, Y. Okawachi, M. Lipson, and A. L. Gaeta, "Octave-spanning mid-infrared supercontinuum generation in silicon nanowaveguides," *Opt. Lett.* **39**, 4518–4521 (2014).
- J. Lu, X. Liu, A. W. Bruch, L. Zhang, J. Wang, J. Yan, and H. X. Tang, "Ultra-violet to mid-infrared supercontinuum generation in single-crystalline aluminum nitride waveguides," *Opt. Lett.* **45**, 4499–4502 (2020).
- X. Liu, A. W. Bruch, J. Lu, Z. Gong, J. B. Surya, L. Zhang, J. Wang, J. Yan, and H. X. Tang, "Beyond 100 THz-spanning ultraviolet frequency combs in a non-centrosymmetric crystalline waveguide," *Nat. Commun.* **10**, 2971 (2019).
- A. Majkić, A. Franke, R. Kirste, R. Schlessler, R. Collazo, Z. Sitar, and M. Zgonik, "Optical nonlinear and electro-optical coefficients in bulk aluminium nitride single crystals," *Phys. Status Solidi B* **254**, 1700077 (2017).
- J. Davila-Rodriguez, A. Ozawa, T. W. Hänsch, and T. Udem, "Doppler cooling trapped ions with a UV frequency comb," *Phys. Rev. Lett.* **116**, 043002 (2016).
- N. Hinkley, J. A. Sherman, N. B. Phillips, M. Schioppo, N. D. Lemke, K. Beloy, M. Pizzocaro, C. W. Oates, and A. D. Ludlow, "An atomic clock with 10^{-18} instability," *Science* **341**, 1215–1218 (2013).
- A. L. Wolf, S. A. van den Berg, W. Ubachs, and K. S. E. Eikema, "Direct frequency comb spectroscopy of trapped ions," *Phys. Rev. Lett.* **102**, 223901 (2009).
- H. Rütz, K.-H. Luo, H. Suche, and C. Silberhorn, "Quantum frequency conversion between infrared and ultraviolet," *Phys. Rev. Appl.* **7**, 024021 (2017).
- K. K. Mehta, C. D. Bruzewicz, R. McConnell, R. J. Ram, J. M. Sage, and J. Chiaverini, "Integrated optical addressing of an ion qubit," *Nat. Nanotechnol.* **11**, 1066–1070 (2016).
- R. L. Sutherland, in *Handbook of Nonlinear Optics*, edited by B. J. Thompson (Marcel Dekker, Inc., New York, Basel, 2006), Vol. 36, p. 964.
- A. V. Syuy, N. V. Sidorov, M. N. Palatnikov, N. A. Teplyakova, D. S. Shtarev, and N. N. Prokopiv, "Optical properties of lithium niobate crystals," *Optik* **156**, 239–246 (2018).
- M. Leidinger, S. Fieberg, N. Waasem, F. Kühnemann, K. Buse, and I. Breunig, "Comparative study on three highly sensitive absorption measurement techniques characterizing lithium niobate over its entire transparent spectral range," *Opt. Express* **23**, 21690–21705 (2015).
- S. Mamoun, A. E. Merad, and L. Guilbert, "Energy band gap and optical properties of lithium niobate from ab initio calculations," *Comput. Mater. Sci.* **79**, 125–131 (2013).
- M. Fukuma and J. Noda, "Optical properties of titanium-diffused LiNbO₃ strip waveguides and their coupling-to-a-fiber characteristics," *Appl. Opt.* **19**, 591–597 (1980).
- T. Nozawa, K. Noguchi, H. Miyazawa, and K. Kawano, "Water vapor effects on optical characteristics in Ti:LiNbO₃ channel waveguides," *Appl. Opt.* **30**, 1085–1089 (1991).
- K. Noguchi, O. Mitomi, and H. Miyazawa, "Millimeter-wave Ti:LiNbO₃ optical modulators," *J. Lightwave Technol.* **16**, 615 (1998).
- J. L. Jackel, C. E. Rice, and J. J. Veselka, "Proton exchange for high-index waveguides in LiNbO₃," *Appl. Phys. Lett.* **41**, 607–608 (1982).

- ²⁵P. G. Suchoski, T. K. Findakly, and F. J. Leonberger, "Stable low-loss proton-exchanged LiNbO₃ waveguide devices with no electro-optic degradation," *Opt. Lett.* **13**, 1050–1052 (1988).
- ²⁶M. L. Bortz and M. M. Fejer, "Annealed proton-exchanged LiNbO₃ waveguides," *Opt. Lett.* **16**, 1844–1846 (1991).
- ²⁷K. R. Parameswaran, R. K. Route, J. R. Kurz, R. V. Roussev, M. M. Fejer, and M. Fujimura, "Highly efficient second-harmonic generation in buried waveguides formed by annealed and reverse proton exchange in periodically poled lithium niobate," *Opt. Lett.* **27**, 179–181 (2002).
- ²⁸C. R. Phillips, C. Langrock, J. S. Pelc, M. M. Fejer, J. Jiang, M. E. Fermann, and I. Hartl, "Supercontinuum generation in quasi-phase-matched LiNbO₃ waveguide pumped by a Tm-doped fiber laser system," *Opt. Lett.* **36**, 3912–3914 (2011).
- ²⁹K. Iwakuni, S. Okubo, O. Tadanaga, H. Inaba, A. Onae, F.-L. Hong, and H. Sasada, "Generation of a frequency comb spanning more than 3.6 octaves from ultraviolet to mid infrared," *Opt. Lett.* **41**, 3980–3983 (2016).
- ³⁰A. S. Kowligy, A. Lind, D. D. Hickstein, D. R. Carlson, H. Timmers, N. Nader, F. C. Cruz, G. Ycas, S. B. Papp, and S. A. Diddams, "Mid-infrared frequency comb generation via cascaded quadratic nonlinearities in quasi-phase-matched waveguides," *Opt. Lett.* **43**, 1678–1681 (2018).
- ³¹M. Zhang, C. Wang, R. Cheng, A. Shams-Ansari, and M. Lončar, "Monolithic ultra-high-q lithium niobate microring resonator," *Optica* **4**, 1536–1537 (2017).
- ³²R. Wolf, I. Breunig, H. Zappe, and K. Buse, "Scattering-loss reduction of ridge waveguides by sidewall polishing," *Opt. Express* **26**, 19815–19820 (2018).
- ³³M. R. Escalé, D. Pohl, A. Sergeev, and R. Grange, "Extreme electro-optic tuning of Bragg mirrors integrated in lithium niobate nanowaveguides," *Opt. Lett.* **43**, 1515–1518 (2018).
- ³⁴Y. He, H. Liang, R. Luo, M. Li, and Q. Lin, "Dispersion engineered high quality lithium niobate microring resonators," *Opt. Express* **26**, 16315–16322 (2018).
- ³⁵C. Wang, M. Zhang, M. Yu, R. Zhu, H. Hu, and M. Lončar, "Monolithic lithium niobate photonic circuits for Kerr frequency comb generation and modulation," *Nat. Commun.* **10**, 978 (2019).
- ³⁶M. Zhang, B. Buscaino, C. Wang, A. Shams-Ansari, C. Reimer, R. Zhu, J. M. Kahn, and M. Lončar, "Broadband electro-optic frequency comb generation in a lithium niobate microring resonator," *Nature* **568**, 373–377 (2019).
- ³⁷J. Lu, J. B. Surya, X. Liu, Y. Xu, and H. X. Tang, "Octave-spanning supercontinuum generation in nanoscale lithium niobate waveguides," *Opt. Lett.* **44**, 1492–1495 (2019).
- ³⁸M. Yu, B. Desiatov, Y. Okawachi, A. L. Gaeta, and M. Lončar, "Coherent two-octave-spanning supercontinuum generation in lithium-niobate waveguides," *Opt. Lett.* **44**, 1222–1225 (2019).
- ³⁹Y. Mengjie, L. Shao, Y. Okawachi, A. L. Gaeta, and M. Lončar, "Ultraviolet to mid-infrared supercontinuum generation in lithium niobate waveguides," in *Conference on Lasers and Electro-Optics (CLEO)* (Optical Society of America, 2020), p. STu4H.1.
- ⁴⁰A. C. Turner, C. Manolatu, B. S. Schmidt, M. Lipson, M. A. Foster, J. E. Sharping, and A. L. Gaeta, "Tailored anomalous group-velocity dispersion in silicon channel waveguides," *Opt. Express* **14**, 4357–4362 (2006).
- ⁴¹Y. Okawachi, M. R. E. Lamont, K. Luke, D. O. Carvalho, M. Yu, M. Lipson, and A. L. Gaeta, "Bandwidth shaping of microresonator-based frequency combs via dispersion engineering," *Opt. Lett.* **39**, 3535–3538 (2014).
- ⁴²J. M. Dudley, G. Genty, and S. Coen, "Supercontinuum generation in photonic crystal fiber," *Rev. Mod. Phys.* **78**, 1135–1184 (2006).
- ⁴³Y. Okawachi, M. Yu, J. Cardenas, X. Ji, M. Lipson, and A. L. Gaeta, "Coherent, directional supercontinuum generation," *Opt. Lett.* **42**, 4466–4469 (2017).
- ⁴⁴A. Rao, K. Abdelsalam, T. Sjaardema, A. Honardoost, G. F. Camacho-Gonzalez, and S. Fathpour, "Actively-monitored periodic-poling in thin-film lithium niobate photonic waveguides with ultrahigh nonlinear conversion efficiency of 4600% W⁻¹ cm⁻²," *Opt. Express* **27**, 25920 (2019).
- ⁴⁵D. D. Hickstein, G. C. Kerber, D. R. Carlson, L. Chang, D. Westly, K. Srinivasan, A. Kowligy, J. E. Bowers, S. A. Diddams, and S. B. Papp, "Quasi-phase-matched supercontinuum generation in photonic waveguides," *Phys. Rev. Lett.* **120**, 053903 (2018).
- ⁴⁶M. Jankowski, C. Langrock, B. Desiatov, A. Marandi, C. Wang, M. Zhang, C. R. Phillips, M. Lončar, and M. M. Fejer, "Ultrabroadband nonlinear optics in nanophotonic periodically poled lithium niobate waveguides," *Optica* **7**, 40 (2020).
- ⁴⁷Y. Furukawa, A. Yokotani, T. Sasaki, H. Yoshida, K. Yoshida, F. Nitanda, and M. Sato, "Investigation of bulk laser damage threshold of lithium niobate single crystals by Q-switched pulse laser," *J. Appl. Phys.* **69**, 3372 (1991).
- ⁴⁸Z. Su, Q. Meng, and B. Zhang, "Analysis on the damage threshold of MgO:LiNbO₃ crystals under multiple femtosecond laser pulses," *Opt. Mater.* **60**, 443–449 (2016).
- ⁴⁹F. Bach, M. Mero, M.-H. Chou, and V. Petrov, "Laser induced damage studies of LiNbO₃ using 1030-nm, ultrashort pulses at 10-1000 kHz," *Opt. Mater. Express* **7**, 240–252 (2017).
- ⁵⁰H. Jiang, R. Luo, H. Liang, X. Chen, Y. Chen, and Q. Lin, "Fast response of photorefractive in lithium niobate microresonators," *Opt. Lett.* **42**, 3267–3270 (2017).
- ⁵¹J. Xu, G. Zhang, F. Li, X. Zhang, Q. Sun, S. Liu, F. Song, Y. Kong, X. Chen, H. Qiao, J. Yao, and Z. Lijuan, "Enhancement of ultraviolet photorefractive in highly magnesium-doped lithium niobate crystals," *Opt. Lett.* **25**, 129–131 (2000).
- ⁵²H. Qiao, J. Xu, G. Zhang, X. Zhang, Q. Sun, and G. Zhang, "Ultraviolet photorefractive features in doped lithium niobate crystals," *Phys. Rev. B* **70**, 094101 (2004).